

Direct numerical simulation of particle-laden flow in a linear compressor cascade: Unsteady boundary-layer effects on blade erosion

Taiyang Wang
HEDPS, CAPT,

School of Mechanics and Engineering Science,
Peking University
Beijing 100871, China
Email: wangtaiyang@stu.pku.edu.cn

Yaomin Zhao*
HEDPS, CAPT,

School of Mechanics and Engineering Science,
Peking University
Beijing 100871, China
Email: yaomin.zhao@pku.edu.cn

ABSTRACT

We perform point-particle direct numerical simulations (PP-DNS) of particle-laden flow through a linear compressor cascade subjected to synthetic freestream turbulence. Monodisperse particles are advanced in a one-way coupled Eulerian-Lagrangian framework with drag-only dynamics. We quantify blade-particle collisions and resulting blade erosion based on high-fidelity data, and the erosion hotspots are predicted near the leading edge and over the pressure side. On the pressure side, for intermediate Stokes numbers, the onset of collisions correlates with elevated boundary-layer intermittency associated with bypass transition, whereas for larger particles impacts occur farther upstream with a higher probability of multiple rebounds. On the suction side, sparse collisions appear only for the smallest particles and are phase-modulated by separation-induced vortex shedding. Joint distributions of impact velocity and angle show that leading-edge impacts are faster and span wider angles than pressure-side impacts, explaining their greater erosive severity. The present results highlight the role of unsteady boundary-layer dynamics in affecting erosion in compressor cascades.

*Address all correspondence to this author.

NOMENCLATURE

Symbols

ρ_f, T_f fluid density and temperature

μ_f, ν_f molecular and kinematic viscosity

U_{in} inlet velocity

τ_w wall shear stress

u_τ wall-friction velocity

ω_z spanwise vorticity

C_{ax} axial chord length

h, L_z blade pitch and the spanwise domain size

τ_f, τ_v characteristic flow time and viscous time scale

C_p, C_f wall-pressure and wall-friction coefficient

Re_f, Ma_f Reynolds and Mach number

Tu, L_s turbulence intensity and integral length scale

γ intermittency

Γ, D logical indicator and detector function

Φ_p volume fraction of the solid phase

ρ_p, d_p, m_p particle density, size and mass

$\mathbf{r}_p, \mathbf{u}_p$ particle position and velocity vectors

τ_p particle relaxation time

C_d drag coefficient

Re_p particle Reynolds number

St, St_v Stokes number and viscous Stokes number

s, n streamwise and wall-normal coordinates

V_p, θ impact velocity and angle

E, ε erosion rate and erosion rate density

1 INTRODUCTION

Solid particle erosion poses a significant threat to gas turbine engines. It can compromise the structural integrity of blades, progressively increase surface roughness, and even alter blade geometry. This

might reduce the lifetime and operational efficiency of engine components, potentially leading to catastrophic failure [1]. Therefore, understanding the effects of particle erosion represents a critical challenge in turbomachinery design.

Early studies on particle erosion in turbomachinery flows were mostly based on experiments. Grant and Tabakoff [2] studied the erosion profiles in a one-and-one-half stage compressor, finding that the leading edge of the rotor undergoes severe erosion. Nevertheless, the photographic methods used in this study limited observations to particles larger than $30\mu\text{m}$ [3]. With the help of laser Doppler velocimeter system, Tabakoff *et al.* [4] investigated the erosive impact of smaller particles, observing that the blade erosion depends significantly on the impact angle. Later, Tabakoff [5] experimentally examined the performance deterioration of a single-stage axial compressor resulting from erosion. It was concluded that the efficiency loss was due to the deterioration of the leading edges as well as changes in the airfoil shape, which was also confirmed by the subsequent study of [6]. Additionally, further evidence of performance deterioration was provided through a series of full-scale engine tests [7, 1]. However, limited by current experimental methods, it is hard to achieve a high-quality synchronous measurement of both fluids and particles [8], which hinders further investigation of particle response to flow fields.

Numerical simulations have become an increasingly important tool for particle-laden flow research due to rapid advancements in computational methods and hardware. For simulations of particle-laden flows, two frameworks are typically employed: one is the Eulerian-Eulerian framework, and the other is the Eulerian-Lagrangian framework [9]. The Eulerian-Eulerian framework, in which both gas and solid phases are treated as continua and the two-fluid model is employed [10], is often criticized for its lack of accuracy, primarily due to its oversimplification of the solid phase and strong reliance on constitutive closures [11, 12, 13]. With the Eulerian-Lagrangian approach, however, the fluid phase is solved within an Eulerian framework, while solid particles are tracked in a Lagrangian manner [14]. Specifically, the forces acting on the particles are determined through fluid-particle interactions, and particle dynamics are governed by Newton's equations of motion [15]. The Eulerian-Lagrangian framework has become the predominant method for investigating gas-particle flows, and numerous numerical simulations have been performed for cases including homogeneous isotropic turbulence [16], planar channel flow [17] and flat-plate boundary layer flow [18, 19, 20].

Under the Eulerian-Lagrangian framework, different strategies can be used for both the gas phase and the particle phase. Regarding the particle phase, most existing studies utilize the point particle approximation, *i.e.* the particles are typically treated as constant-density spheres and are assumed to be smaller than the Kolmogorov length scale [9, 14]. Compared to particle resolved simulations in which the flow fields

around particles need to be fully resolved, simulations with point particles require much less computational resources. For the gas phase, the flow field can be calculated using Reynolds-averaged Navier-Stokes (RANS), large-eddy simulation (LES) or direct numerical simulations (DNS). However, the turbulence models introduced in RANS and LES may cause unphysical effects [21], casting doubt on their applicability when simulating complex phenomena such as flow separation and transition. In comparison, the point-particle direct numerical simulation (PP-DNS), in which the turbulent flow is fully resolved rather than modeled, has been demonstrated to be an indispensable method for its effectiveness in investigating the statistical behavior of particles [15, 14]. Nevertheless, existing PP-DNS studies mainly focus on canonical cases with simple geometries, and applications to turbomachinery geometries remain scarce.

Focusing on turbomachinery erosion, Tabakoff and coworkers conducted a number of pioneering simulations [22, 23]. Because the volume fraction of the solid phase ϕ_p in engine-relevant gas-solid mixtures is typically below 10^{-6} [24], their studies adopted the one-way coupling strategy, which neglects the feedback of the solid phase on the fluid phase [14]. Nevertheless, these early studies were restricted to two-dimensional scenarios and treated the flow as inviscid. Subsequently, a majority of studies were conducted based on three-dimensional RANS [25, 26, 8], where a partitioned method was employed: a time-averaged flow field is first computed, and particles are then propagated through it in a subsequent step. Although this strategy significantly reduces computational resource requirements, the steady assumption of turbomachinery flows is often unrealistic [27]. This shortcoming was addressed by Beck *et al.* [28], who performed the first particle-laden turbomachinery flow based on LES approach. The LES simulation, however, introduces turbulence models to account for the sub-grid scale fluctuations, thus the response of particles to turbulence cannot be accurately captured [29, 30]. Therefore, to enable a deeper investigation of particle behaviors in real turbomachinery applications, simulations that resolve all turbulent scales are necessary. However, to the best of the authors' knowledge, no high-fidelity database for particle-laden turbomachinery flows based on PP-DNS has been published.

In the present study, we perform PP-DNS of particle-laden flow through a linear compressor cascade subjected to controlled freestream turbulence. The fully resolved blade boundary layers enable a mechanistic assessment of how unsteady phenomena, bypass transition on the pressure side and separation-induced shedding on the suction side, govern particle-wall collisions and ensuing erosion. We consider monodisperse particles at three Stokes numbers within the point-particle regime and quantify (i) collision statistics and spatial distributions, (ii) their correlation with boundary-layer intermittency and shedding dynamics, and (iii) the resulting erosion via Oka's model [31]. To our knowledge, this constitutes the first PP-DNS database

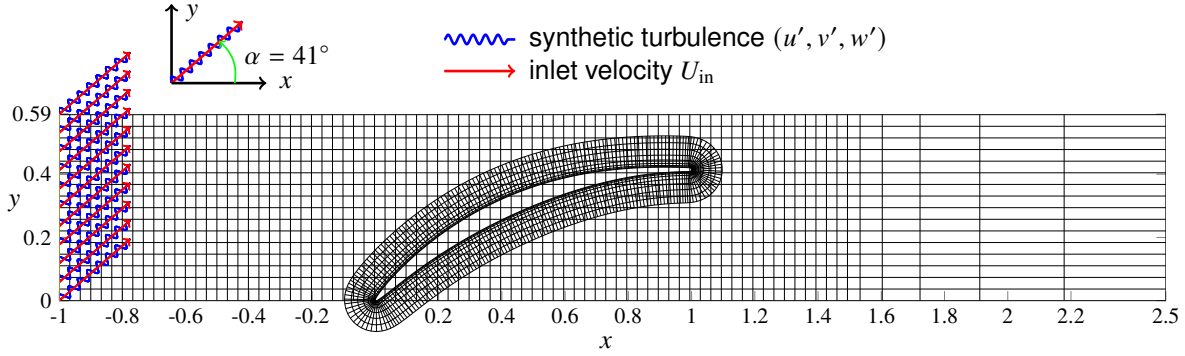


Fig. 1. Schematic of the axial and pitchwise $(x-y)$ plane of the particle-laden flow in a linear compressor cascade: the computational grid consists of a background H-type grid and an O-type grid, which is shown about every sixteenth line in each direction.

of blade-particle interactions in a turbomachinery geometry.

2 NUMERICAL SIMULATION

The primary objective of this study is to examine the erosive impact of varying-size sand particles on a compressor blade surface by means of PP-DNS. For simplicity, the volume fraction of sand particles is assumed to be sufficiently low to adopt the one-way coupling strategy, thus the motion of the solid phase is driven by the gas phase with no feedback mechanism [14]. In the following, the numerical treatment and setup for both two phases are discussed in detail.

2.1 Gas Phase

For the flow simulation, a linear compressor cascade with the NACA 65 blade profile is assumed to operate at room temperature. Based on the inlet velocity, the operating axial Reynolds number is $Re_f = 138,500$ and the Mach number is $Ma_f = 0.15$, corresponding to the previous work of Zaki *et al.* [32]. The resulting unsteady flow field is obtained by solving the three-dimensional compressible Navier-Stokes equations using the solver HiPSTAR [33].

Figure 1 shows a schematic of the numerical setup. The usage of the overset grid method [34] requires a hybrid H-O type grid, whose detailed parameters are provided in Table 1. The present DNS is conducted in a Cartesian coordinate system (x, y, z) , where the coordinates x , y and z correspond to the axial, pitchwise,

Table 1. Grid parameters.

Grid	N_x	N_y	L_z	N_z	Points
H-type grid	1540	337	0.24	160	83,036,800
O-type grid	2152	137	0.24	160	47,171,840

and spanwise directions, respectively. The background H-type grid governs the computational domain, which spans one blade pitch $h = 0.59C_{ax}$ in the pitchwise direction and has a spanwise extent of $L_z = 0.24C_{ax}$. Here, $C_{ax} = 1$ is the non-dimensional axial chord length. Besides, periodic boundary conditions are applied in both the pitchwise and spanwise directions. The O-type grid ensures accurate resolution of the blade boundary layer, with an adiabatic, no-slip blade surface. At the inlet, a uniform velocity condition $(U_{in} \cos(\alpha), U_{in} \sin(\alpha), 0)$ is imposed, as indicated by the red arrow in Fig. 1. Here, $U_{in} = 1$ is the non-dimensional inlet velocity and $\alpha = 41^\circ$ is the angle of attack. To replicate realistic incoming turbulence, synthetic free-stream turbulence (FST) symbolized by the blue wavy line is generated at the inlet using a digital filter approach [35, 36]. The turbulence intensity is $Tu = 3.25\%U_{in}$ and the integral length scale is $L_s = 0.06C_{ax}$, the same as the previous study of [32]. In addition, a characteristic boundary condition combined with a sponge layer is applied at the outlet to prevent spurious reflections [37].

In the present cases, the grid spacings around the blade surface, normalized by the viscous scale, are below (9, 0.8, 10) in the streamwise, wall-normal and spanwise directions, respectively. The resolution is similar to previous DNS cases [32] and considered sufficient to resolve the blade boundary layer. Thus the present DNS flow fields can be served as a basis to subsequent Lagrangian particle tracking.

2.2 Solid Phase

For the solid phase, the physical models, numerical strategies and parameter setup are discussed below. The sand particles are modeled as point particles, idealized as rigid spheres with a uniform diameter d_p and density ρ_p . The non-dimensional equations of motion for these Lagrangian particles are given by [19]

$$\begin{aligned} \frac{d\mathbf{r}_p}{dt} &= \mathbf{u}_p, \\ m_p \frac{d\mathbf{u}_p}{dt} &= \mathbf{f}_{drag}, \end{aligned} \quad (1)$$

where \mathbf{r}_p and \mathbf{u}_p represent the position and velocity vectors of each particle, respectively, and $m_p = \pi\rho_p d_p^3/6$ is the particle mass. Owing to the significantly higher density of the solid phase compared to the gas phase, only the drag force \mathbf{f}_{drag} [38] is considered, given by

$$\mathbf{f}_{drag} = 3\pi\mu_f d_p \frac{C_d}{24} \frac{Re_p}{Re_f} (\mathbf{u}_f - \mathbf{u}_p), \quad (2)$$

where \mathbf{u}_f represents the fluid velocity at the particle's center of mass. Besides, μ_f is the fluid dynamic viscosity, which depends on the local temperature T_f via Sutherland's law [39]

$$\mu_f = T_f^{3/2} \frac{1 + C_{\text{Suth}}}{T_f + C_{\text{Suth}}}. \quad (3)$$

Here, C_{Suth} is the Sutherland's constant. Moreover, $Re_p = Re_f |\mathbf{u}_f - \mathbf{u}_p| d_p / \nu_f$ is the particle Reynolds number, where ν_f is the fluid kinematic viscosity. In addition, C_d is the drag coefficient [40], which is calculated with

$$C_d = \begin{cases} \frac{24}{Re_p} (1 + 0.15 Re_p^{0.687}) & Re_p \leq 1000, \\ 0.44 & Re_p > 1000. \end{cases} \quad (4)$$

Note that particles moving in turbomachinery flows may also undergo the influence of other forces, such as the Saffman lift force [41, 42] resulted by the strong vorticity. Nevertheless, their effects are ignored in the present study for simplicity.

The particle motion equations (1) are calculated using the velocity Verlet algorithm [43, 44]:

$$\begin{aligned} \mathbf{r}_p(t + \Delta t) &= \mathbf{r}_p(t) + \Delta t \mathbf{u}_p + \frac{\Delta t^2}{2m_p} \mathbf{f}_{\text{drag}}(t), \\ \mathbf{u}_p(t + \Delta t) &= \mathbf{u}_p(t) + \frac{\Delta t}{2m_p} [\mathbf{f}_{\text{drag}}(t) + \mathbf{f}_{\text{drag}}(t + \Delta t)], \end{aligned} \quad (5)$$

where Δt is the time step. Besides, $\mathbf{f}_{\text{drag}}(t + \Delta t)$ represents the drag force computed based on the particle position at time $(t + \Delta t)$, and required flow variables at the particle location are obtained through trilinear interpolation [18, 20]. Additionally, particle-blade interactions are handled using a hard-sphere collision model, and a collision is detected when the particle's center of mass is located inside the blade geometry [45]. During the rebound process, the finite size of the particle is ignored, and collisions with the curved blade surface are treated with a mirror symmetry condition relative to the local surface tangent plane.

Different from a majority of particle-laden simulations confined to single rectangular grid, the present simulations are conducted within a hybrid H-O grid with overlapping zones. This complex topology and geometry pose a significant computational challenge to the efficient tracking of numerous particle trajec-

ries, especially the tracking in the curved O-type grid. To address this, we propose a robust and efficient framework based on overlapping grids [46], and large-scale direct numerical simulations thus become feasible. Besides, a wide range of cases has been simulated to validate the accuracy and effectiveness of the proposed framework, and more details regarding the numerical implementations can be found in [46].

Subsequently, physical parameters of the solid phase are defined. The sand particles are assumed to be composed of calcia-magnesia-alumina-silicate (CMAS) [47], and the density is set as $\rho_p^* = 2690 \text{ kg/m}^3$. Satisfying the point-particle assumption [9], the particle diameter d_p^* is set to be smaller than the Kolmogorov scale $\eta_f^* \approx 4.5 \mu\text{m}$. Accordingly, three cases with different particle sizes are established, and detailed parameters are summarized in Table 2. Moreover, the Stokes number $St = \tau_p/\tau_f$ is introduced to characterize particle behavior, which is defined as the ratio of the particle relaxation time τ_p to a characteristic flow time τ_f . Here, τ_p is calculated as $\tau_p = Re_f \rho_p d_p^2 / (18\mu_f)$, and $\tau_f = C_{ax}/U_{in}$ is defined as the ratio of the axial chord length to inlet velocity.

Furthermore, to simulate the continuous ingestion of sand, particles are injected into the computational domain. Numerically, at every non-dimensional time interval $\Delta t_{add} = 0.012$, a total of $N_{add} = 1755$ particles are emitted from fixed positions, which are uniformly distributed at the inlet. The initial particle velocity is set to match the local fluid velocity, obtained via interpolation from the surrounding flow field. Besides, particles that travel beyond the region $x > 1.65$ are removed from the simulation to save computational costs. Under this setup, there are approximately 6×10^5 particles in the computational domain at the statistically steady state, resulting in a solid-phase volume fraction of $\Phi_p < 10^{-6}$, which satisfies the criterion for the one-way coupling strategy [24]. Moreover, data is collected over a time period of $9.2C_{ax}/U_{in}$ for subsequent analyses.

3 RESULTS

3.1 Overview of the Particle-Laden Flow Field

We first present the mean statistics of the blade boundary layer in Fig. 2. The pressure coefficient is defined as $C_p = (p_w - p_0)/(0.5\rho_{in}U_{in}^2)$, where p_w denotes the wall pressure and p_0 is a reference pressure;

Table 2. Parameters for particle-laden compressor flow cases.

Cases	$\rho_p^* (\text{kg/m}^3)$	$d_p^* (\mu\text{m})$	d_p^*/η_f^*	St
case d1	2690	1	0.2267	0.0101
case d2	2690	2	0.4534	0.0403
case d4	2690	4	0.9067	0.1612

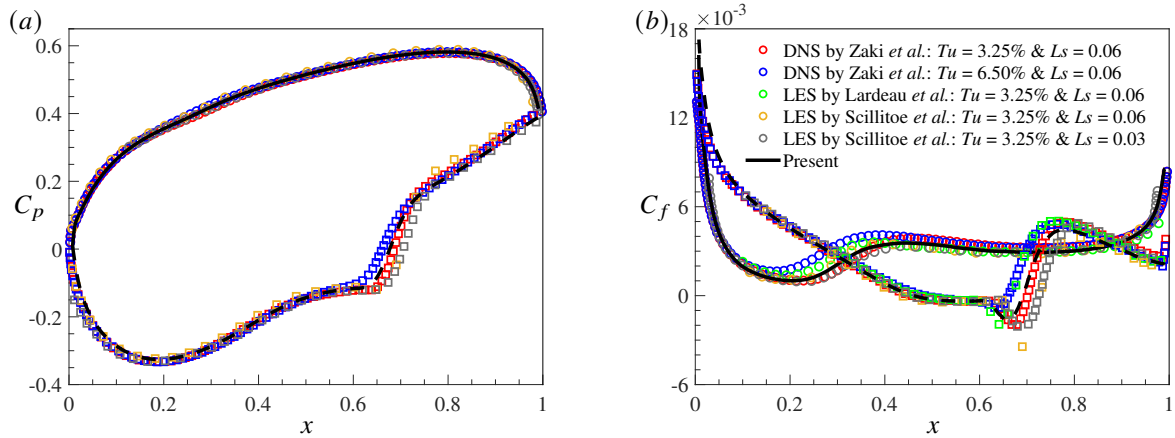


Fig. 2. Statistics of the boundary layer around the blade surface: (a) wall-pressure coefficient C_p ; (b) wall-friction coefficient C_f . Here, the results on the pressure side are denoted by circles and solid lines, while the results on the suction side are denoted by squares and dashed lines.

while the wall-friction coefficient C_f is defined as $C_f = \tau_w / (0.5\rho_{in}U_{in}^2)$, where τ_w is the wall shear stress. The distributions of C_p and C_f around the blade are shown in Fig. 2(a) and Fig. 2(b), respectively. On the pressure side as represented by the solid lines, the blade boundary layer experiences an adverse pressure gradient (APG) starting from the leading edge ($0 < x \lesssim 0.8$), followed by a favorable pressure gradient (FPG) at $0.8 \lesssim x$. In the APG region, the C_f features an increase from $x \approx 0.2$ to $x \approx 0.4$, suggesting boundary layer transition from laminar to turbulent state. Moreover, the pressure-side boundary layer flow accelerates in the FPG region, and the C_f value further increases accordingly at $0.8 \lesssim x$. On the suction side, the blade boundary layer first undergoes an FPG, which is then followed by a severe APG ($0.2 \lesssim x$). The strong APG causes the boundary layer to separate, forming a large separation region at $x \approx 0.46 \sim 0.69$ as evidenced by the negative wall-friction coefficient $C_f < 0$ in Fig. 2(b). Downstream of the separation, flow reattaches due to transition to turbulence, as suggested by the sudden increase of C_f at around $x \approx 0.7$. Importantly, both the wall-pressure and wall-friction coefficients from the present simulations show good agreements with previous results[32, 48, 49, 50], as indicated by the comparison between the lines and symbols. The slight discrepancies among these cases, however, are presumably resulted by the differences in synthetic methods for generating the incoming FST.

We further visualize the particle-laden flow fields in Fig. 3, providing an overview of the flow structures and particle distribution by an instantaneous snapshot in the $(x - y)$ plane for each case. For the gas phase, the boundary layer transition are clearly shown by the emergence of abundant vortical structures identified by the Q criterion [51], while the flow separation on the suction side is identified by the green lines. Furthermore, for the solid phase, particles denoted by brown spheres convect downstream through

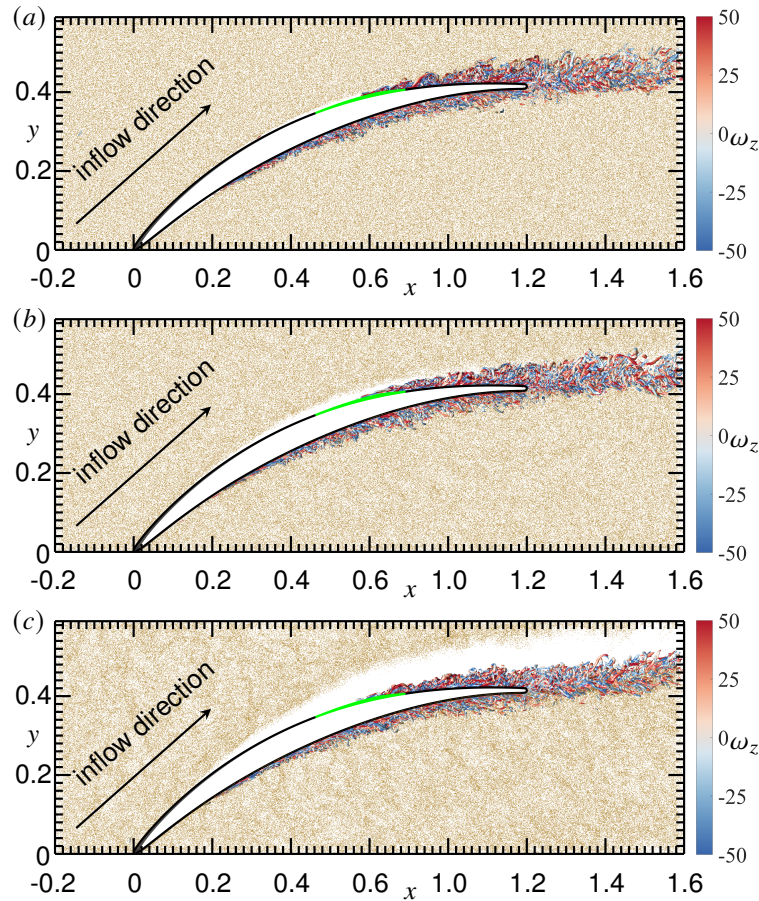


Fig. 3. An axial and pitchwise ($x-y$) overview of (a): case d1; (b): case d2; (c): case d4. Here, sand particles are denoted brown spheres, and vortical structures identified by Q criterion are presented, which are colored by the spanwise vorticity ω_z . Moreover, the inflow direction is marked by the black arrow, and the mean separation region is denoted by the green line.

the passage. During this process, many particles interact with transitional and turbulent flow structures, undergoing a modulation effect of the flow unsteadiness. For example, on the suction side, particles in case d1 are able to interact with vortices shed from the separation region, as shown in Fig. 3(a). As the St number increases, particle inertia gradually dominates, resulting in less directional variation of particle velocity. Therefore, fewer particles enter the suction-side boundary layer, as indicated by the wider particle-free (blank) regions in Figs. 3(b) and 3(c). In comparison, the pressure-side boundary layer is populated with particles across all cases, suggesting more frequent particle-blade interactions.

3.2 Erosion by Blade-Particle Collisions

3.2.1 Collision Locations and frequencies

Focusing on the erosion caused by blade-particle collisions, we first examine the spatial distribution of collisions over the surface, and the results are presented in Fig. 4. We can see that the vicinity of blade leading edge experiences severe particle impacts, and the affected region expands downstream on both sides as the St number increases. On the pressure side, collisions in case d1 are mainly scattered within the mid-chord region, as shown in Fig. 4(a). For case d2 shown in Fig. 4(c), a clear line divides the impacted and non-impacted zones, which is likely attributable to the occurrence of transition. Besides, the number of collision events has increased significantly. Moreover, collisions in case d4 occur over the entire pressure side as presented in Fig. 4(e), which is presumably because the particles with large inertia show ballistic-like trajectories. On the suction side, sparse collisions are observed downstream the mean separation region, as exhibited in Fig. 4(b). Notably, this phenomenon does not occur in other two cases at the same region, consistent with the absence of particles revealed in Figs. 3(b) and 3(c).

To further quantify the blade-particle collisions, we present the x distribution of the time-averaged collision rate in Fig. 5. We can observe that the collision rate in the leading edge is featured as a peak value, whose width becomes wider as the St number increases, corresponding to the enlargement of the erosion region at the leading edge as shown in Fig. 4. On the pressure side, with the increase of St number, the collision frequency is significantly increased. Notably, case d4 is featured as high collision frequency all over the pressure-side blade, while the collision rate of case d2 exhibits a sudden increase at $x \approx 0.25$. Moreover, the case d1 shows visible particle-blade collisions in limited regions at $0.35 \lesssim x \lesssim 0.45$, suggesting that the transitional flow structures in this region might cause strong wall-normal transport of low-inertia particles. On the suction side, collisions are mainly detected in case d1 from $x \approx 0.8$ and the frequency is very low, while no collisions are observed for the other two cases.

3.2.2 Particle Responses to Flow Unsteadiness

To elucidate the underlying mechanisms for the different collision distributions in the present cases, a detailed investigation of particle response to flow unsteadiness is undertaken. Based on the different transition mechanisms on the pressure and suction sides [32], the flow unsteadiness is divided into two types: one is the bypass transition to turbulence on the pressure side, and the other is the unsteady vortex shedding induced by flow separation on the suction side.

The boundary layer transition can be characterized by intermittent flows structures developing into

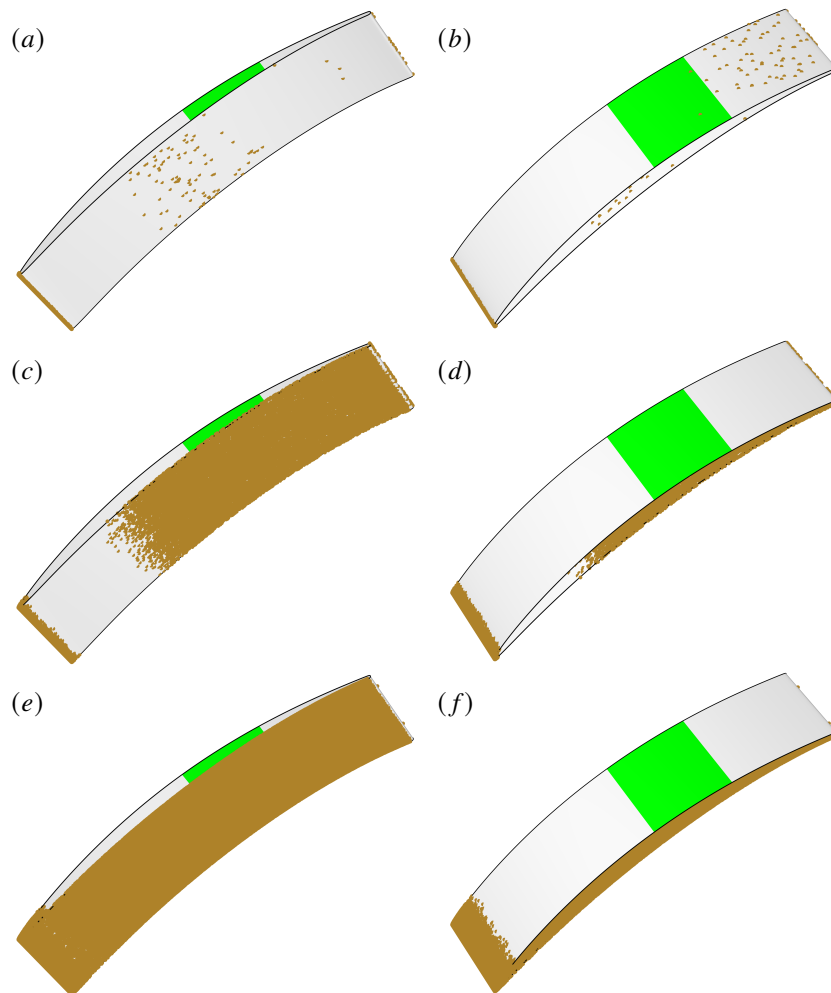


Fig. 4. Particles which impact the blade for (a, b): case d1; (c, d): case d2; (e, f): case d4. Here, the left three figures correspond to the results on the pressure side, while right three figures correspond to the results on the suction side. Besides, the mean separation region is marked by the green surface, and sand particles are denoted by brown spheres.

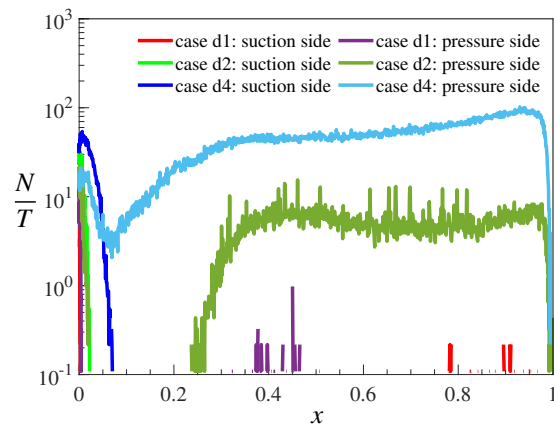


Fig. 5. The x distribution of the time-averaged collision rate.

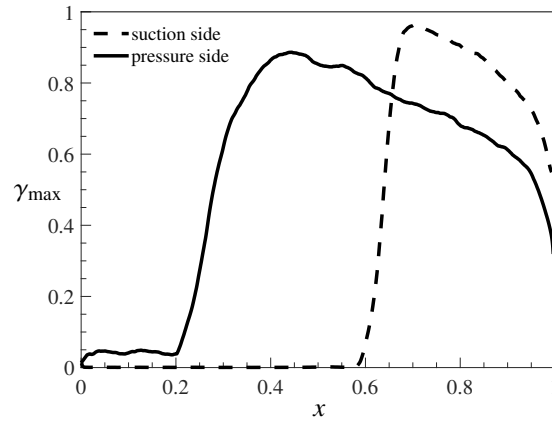


Fig. 6. Peak intermittency around the boundary layer.

turbulence, which can be quantified by the intermittency factor γ , which indicates the possibility that the local flow is turbulent. Following the discrimination algorithm proposed by Nolan and Zaki [52], the calculation procedure is summarized as follows. First, a detector function D is defined as the sum of absolute values of wall-normal and spanwise velocity fluctuations, namely $D = |u'_{f,n}| + |u'_{f,z}|$. Then, a local standard deviation filter is applied to the D field using a three-dimensional stencil [53]. Moreover, at each wall-normal location n , a threshold for the filtered data is determined using Otsu's method [54]. The turbulent region is defined as where the filtered value exceeds this threshold, corresponding to a logical indicator function $\Gamma = 1$; the non-turbulent region is where the value is below the threshold, and $\Gamma = 0$. Subsequently, the mean intermittency γ is obtained by averaging Γ over the spanwise direction and time,

$$\gamma(x, n) = \frac{1}{TL_z} \int_0^{L_z} \int_{t_0}^{t_0+T} \Gamma dt dz. \quad (6)$$

Furthermore, the maximum intermittency in the wall-normal direction is evaluated,

$$\gamma_{\max}(x) = \max_n(\gamma), \quad (7)$$

and the results are shown in Fig. 6.

Based on the intermittency plot, the pressure side is divided into three regions: laminar region ($0 < x \lesssim 0.2$) featured as a relatively low level γ_{\max} , transitional region ($0.2 \lesssim x \lesssim 0.45$) characterized by a remarkable

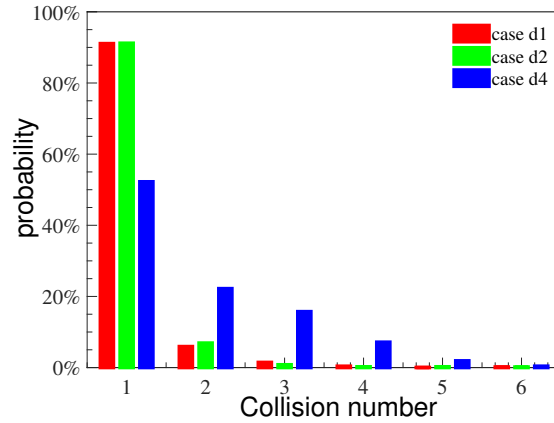


Fig. 7. Probability of blade-particle collision number for each case. For particles colliding with the blade, the number of collisions happened for each particle are collected for statistics.

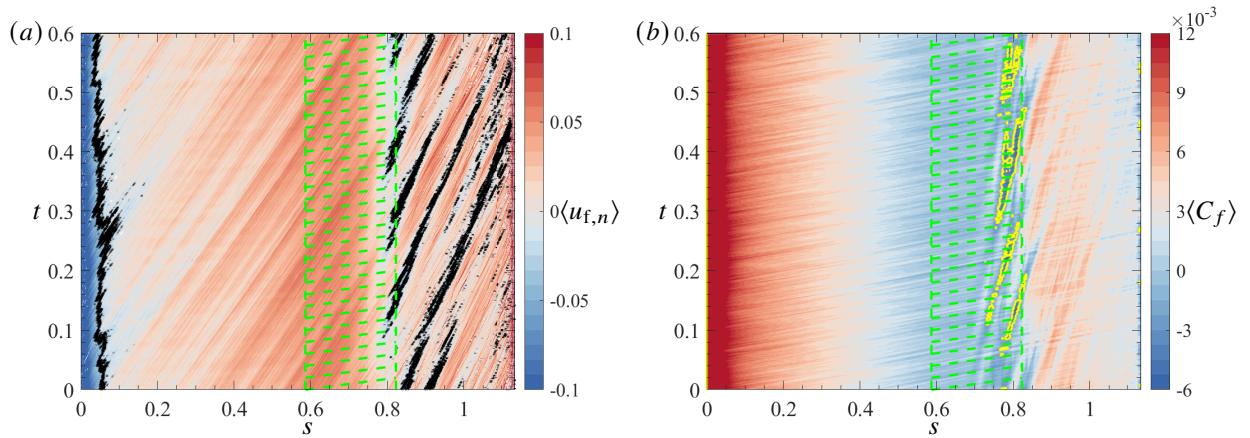


Fig. 8. Temporal and spatial distribution of spanwise-averaged (a) wall-normal velocity of particle and (b) instantaneous wall-friction coefficient along the blade surface, where s represents the arc-length from the leading edge. The particle data set is selected as the layer normal to the blade surface at a distance of $n \in [0.02, 0.04]$. In both two figures, the region filled by green dashed lines indicate the mean separation area. Besides, black lines in Fig. 8(a) correspond to the contour $\langle u_{p,n} \rangle = -0.03$, the yellow lines in Fig. 8(b) correspond to the contour $\langle C_f \rangle = -0.003$.

increase of γ_{\max} and turbulent region ($0.45 \lesssim x < 1$) featured as a relatively high level γ_{\max} . It is noted that the sudden increase of the collision rate for case d2 shown in Fig. 5 is closely related to the transition onset $x \approx 0.2$. Moreover, particles with a small St number in case d1 show collisions predominantly within the range ($0.35 \lesssim x \lesssim 0.45$), in which the γ_{\max} shows very large value. The coincidence of the onset of transition and collisions in case d2 suggests that collisions on the pressure side are correlated with the perturbations resulting from transition to turbulence. Nevertheless, this conclusion does not hold true for case d4, wherein particles with larger inertia tend to ballistic trajectories, and the particle-blade collision happens all over the pressure-side surface. On the suction side, the intermittency shows an increase at

$0.6 \lesssim x \lesssim 0.7$ in Fig. 6. As previously discussed, collisions on this side occur only in case d1, and most of them start from $x \approx 0.8$, lagging behind the transition onset point $x \approx 0.6$. This discrepancy suggests that the collisions are not directly caused by the transition process itself. Instead, it is presumably resulted by the response of particles to violent vortex shedding behaviors induced by flow separation.

Furthermore, we evaluate the particle response to flow unsteadiness by the number of collisions for each particle [28], and results are presented in Fig. 7. Considering the fact that collision events predominantly occur on the pressure side, we only present the collision number of the pressure-side boundary layer accordingly. As shown in Fig. 7, for cases d1 and d2, the vast majority of particles collide with the pressure-side surface only once. However, this trend does not hold for case d4, where the probability of multiple collisions increases significantly. The multiple collision in case d4 suggests that the particles show a stronger response to turbulent fluctuations in the boundary layer. Hereafter, we further evaluate the viscous Stokes number $St_v = \tau_p/\tau_v$. Defining the characteristic flow time as the mean viscous time scale over the pressure-side boundary layer $\tau_v = \nu_f/u_\tau$, where $u_\tau = \sqrt{\tau_w/\rho_f}$ is the wall-friction velocity, the resulting viscous Stokes numbers St_v , for cases d1, d2 and d4 are approximately 1.7656, 7.0449 and 28.1796, respectively. Notably, the St_v value in case d4 is very close to 30, which is suggested to be one indicator that the according particles tend to exhibit more pronounced concentration phenomena in turbulent channel flows [55, 17]. This phenomenon was suggested to be resulted by the more remarkable particle flux towards the wall, which is greatly affected by turbulent flow structures. Therefore, it is inferred that particles in case d4 show stronger responses to turbulent structures and more particles tend to move towards the blade surface, leading to the higher incidence of multiple collisions for each particle.

Moreover, to reveal the particle response to separation-induced vortex shedding events, we examine the temporal and spatial evolution of the spanwise-averaged wall-normal particle velocity $\langle u_{f,n} \rangle$ and wall-friction coefficient $\langle C_f \rangle$, as shown in Figs. 8(a) and 8(b), respectively. Downstream the mean separation region, particles undergo periodic up-and-down movements as they travel downstream, as indicated by alternating stripes of positive and negative values in the $\langle u_{p,n} \rangle$ contour plot. Notably, contour $\langle C_f \rangle = -0.003$ in Fig. 8(b) exhibits stripe-like patterns with a similar frequency and slope. This strong spatio-temporal correlation leads us to conclude that particle movements are significantly modulated by unsteady vortex shedding behaviors. Presumably resulted from abundant shedding vortices, some particles are gradually transported to the near-wall region as indicated by the contour $\langle u_{f,n} \rangle = -0.03$ in Fig. 8(a), leading to collisions.

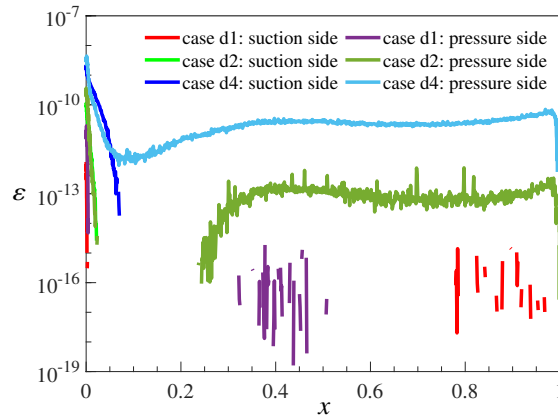


Fig. 9. The x distribution of the erosion rate density per unit time ε .

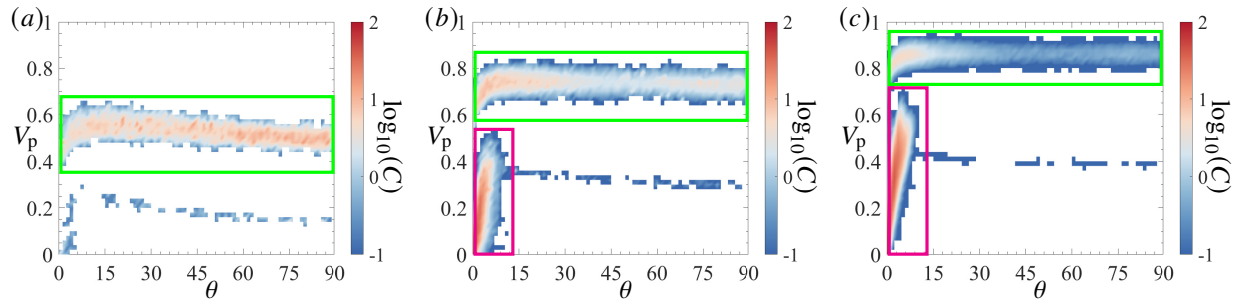


Fig. 10. The joint probability distribution function of particle's impact velocity V_p and impact angle θ upon erosion on the blade surface for (a): case d1; (b): case d2; (c): case d4. Here, green boxes mark collision events occurring near the leading edge; magenta boxes mark collisions on the pressure side.

3.2.3 Erosion Intensity

To quantify the erosion effects of particles on the blade, we model the blade-particle collisions as the erosion of sand particles to steel, and employ the widely adopted Oka erosion model [31]. This model defines the erosion rate E as the mass of wall material removed per unit mass of impacting particles, which is given by

$$E = E_{90} \left(\frac{V_p^*}{V_{\text{ref}}} \right)^{k_2} \left(\frac{d_p^*}{d_{\text{ref}}} \right)^{k_3} f(\theta). \quad (8)$$

Here, E_{90} is the reference erosion rate at 90° , V_p^* is the impact velocity of particles, V_{ref} is the reference velocity, d_{ref} is the reference diameter, k_2 and k_3 are velocity and diameter exponents, respectively. Besides,

$f(\theta)$ is the function of the impact angle θ , which is given by

$$f(\theta) = (\sin \theta)^{n_1} [1 + H_v(1 - \sin \theta)]^{n_2}. \quad (9)$$

Here, H_v is the wall material Vickers hardness (GPa), n_1 and n_2 are angle function constants. For a sand-steel system, the parameters are set according to the theory guide of Ansys Fluent 2021 R2: $E_{90} = 6.15 \times 10^{-4}$, $V_{\text{ref}} = 104\text{m/s}$, $d_{\text{ref}} = 326\mu\text{m}$, $k_2 = 2.35$, $k_3 = 0.19$, $H_v = 1.8\text{GPa}$, $n_1 = 0.8$, $n_2 = 1.3$. Moreover, the overall damage to the blade is assessed by the erosion rate density per unit time, ε (mg/s·mm²), which is defined as

$$\varepsilon = \frac{1}{A^*} \sum_{i=1}^{n_i} m_p^* E_i. \quad (10)$$

Here, n_i is the number of impacting particles per unit time (s) and A^* is the local surface area (mm²).

The spatial distribution of ε is presented in Fig. 9. For cases d1 and d2, the most severe erosion occurs at the leading edge, corresponding to the peak collision rate presented in Fig. 5. Similarly, though the majority of collisions occur on the pressure side in case d4, the resulting erosion is much weaker than that on the leading edge. This is because, in addition to collision number, both the impact velocity and angle play an important role in blade erosion. Therefore, we further examine the according joint probability distribution function (PDF) in Fig. 10. For case d1, the PDF predominantly exhibits a horizontal stripe pattern characterized by a nearly constant impact velocity, which is marked by the green box. This pattern is obviously resulted by collision events occurring near the leading edge. Moreover, for cases d2 and d4, a distinct oblique stripe pattern marked by the magenta box emerges from the origin, corresponding to a mount of additional collision events occurring on the pressure side. By comparison, it is observed that collisions near the leading edge involve relatively high impact velocities and span a wide range of impact angles, while the pressure-side collisions manifest relatively low impact velocities and small impact angles. These characteristics further explain why the most severe erosion occurs on the leading edge, as discussed earlier.

4 CONCLUSIONS

We performed point-particle direct numerical simulations (PP-DNS) of sand-laden flow through a linear compressor cascade subjected to controlled freestream turbulence and quantified blade erosion using Oka's model. The DNS reproduces key boundary-layer features reported in the literature, including pressure-side bypass transition and suction-side separation with reattachment, thereby providing a credible baseline for assessing particle-wall interactions.

Erosion hotspots are predicted at the leading edge and on the pressure side. Although the pressure side experiences more frequent particle-wall collisions, the leading edge exhibits the highest erosion severity due to larger impact velocities and a broader distribution of impact angles. On the pressure side, the onset and distribution of impacts are governed by the interplay between particle inertia and transitional dynamics. For small Stokes numbers, impacts are scarce upstream and emerge after boundary-layer intermittency increases during bypass transition, indicating a tight coupling between transitional perturbations and near-wall particle transport. For intermediate Stokes numbers, the onset of frequent impacts shifts upstream and aligns with the location of rapid growth in intermittency. For the largest Stokes number examined, particle trajectories are increasingly ballistic-like, collisions occur over most of the pressure side, and the probability of multiple rebounds rises markedly. The corresponding viscous Stokes number, $St_\nu \approx 28$, is consistent with enhanced near-wall concentration tendencies reported in canonical turbulent wall flows. On the suction side, rare impacts are observed only for the smallest particles, mostly downstream of the mean separation bubble. Space-time correlations between spanwise-averaged wall friction and particle wall-normal velocity demonstrate that separation-induced vortex shedding modulates the timing and location of these impacts. Furthermore, joint distributions of impact velocity and angle further differentiate leading-edge and pressure-side erosion mechanisms: leading-edge impacts combine higher speeds with a wide range of angles, whereas pressure-side impacts cluster at lower speeds and shallower angles.

The present simulations are conducted based on the assumption that particles are subject solely to the drag force. This assumption needs to be examined in future study, since the complex operation conditions in modern aircraft engines may cause additional forces, such as the pressure gradient force, Saffman lift force and so on. Besides, more complicated blade-particle interaction models, such as the soft-sphere model considering the deformation of particles, can be adopted in further studies for more realistic effects. Nevertheless, the findings obtained from the present study, particularly the modulation of the erosion patterns by the transitional intermittency and separation-induced shedding, provide physically grounded insights for turbomachinery erosion assessment. This enables improved hotspot identification and durability

prediction in particle-laden operating environments. Moreover, by resolving all turbulent scales, the present high-fidelity database offers a benchmark for the systematic calibration and validation of engineering-scale erosion models, suggesting longstanding engineering impacts.

ACKNOWLEDGEMENTS

The authors wish to thank Prof. Richard D. Sandberg for the license of using the code HiPSTAR. This work has been supported by the National Natural Science Foundation of China (Grant Nos. 12588201, 12432010, and 12572247).

REFERENCES

- [1] Dunn, M. G., 2012, "Operation of gas turbine engines in an environment contaminated with volcanic ash," *ASME J. Turbomach.*, **134**(5), 05, p. 051001.
- [2] Grant, G., and Tabakoff, W., 1975, "Erosion prediction in turbomachinery resulting from environmental solid particles," *J. Aircraft*, **12**(5), pp. 471–478.
- [3] Hamed, A., Tabakoff, W. C., and Wenglarz, R., 2006, "Erosion and deposition in turbomachinery," *J. Propuls. Power.*, **22**(2), pp. 350–360.
- [4] Tabakoff, W., Malak, M. F., and Hamed, A., 1987, "Laser measurements of solid-particle rebound parameters impacting on 2024 aluminum and 6a1-4v titanium alloys," *AIAA J.*, **25**(5), pp. 721–726.
- [5] Tabakoff, W., 1987, "Study of single-stage axial flow compressor performance deterioration," *Wear*, **119**(1), pp. 51–61.
- [6] Ghenaïet, A., Tan, S. C., and Elder, R. L., 2004, "Experimental investigation of axial fan erosion and performance degradation," *Proc. Inst. Mech. Eng. A: J. Power Energy*, **218**(6), pp. 437–450.
- [7] Dunn, M. G., Padova, C., Moller, J. E., and Adams, R. M., 1987, "Performance deterioration of a turbofan and a turbojet engine upon exposure to a dust environment," *J. Eng. Gas. Turbine. Power.*, **109**(3), 07, pp. 336–343.
- [8] Ghenaïet, A., 2024, "Modeling and simulation of sand particle trajectories and erosion in a transonic fan stage," *ASME J. Turbomach.*, **147**(7), 12, p. 071012.
- [9] Balachandar, S., and Eaton, J. K., 2010, "Turbulent dispersed multiphase flow," *Ann. Rev. Fluid Mech.*, **42**, pp. 111–133.
- [10] Baer, M., and Nunziato, J., 1986, "A two-phase mixture theory for the deflagration-to-detonation transition (ddt) in reactive granular materials," *Int. J. Multiphase Flow*, **12**(6), pp. 861–889.

- [11] Slater, S. A., and Young, J. B., 2001, "The calculation of inertial particle transport in dilute gas-particle flows," *Int. J. Multiphase Flow*, **27**(1), pp. 61–87.
- [12] Slater, S., Leeming, A., and Young, J., 2003, "Particle deposition from two-dimensional turbulent gas flows," *Int. J. Multiphase Flow*, **29**(5), pp. 721–750.
- [13] Sundaresan, S., Ozel, A., and Kolehmainen, J., 2018, "Toward constitutive models for momentum, species, and energy transport in gas–particle flows," *Annu. Rev. Chem. Biomol. Eng.*, **9**, pp. 61–81.
- [14] Brandt, L., and Coletti, F., 2022, "Particle-laden turbulence: Progress and perspectives," *Ann. Rev. Fluid Mech.*, **54**, pp. 159–189.
- [15] Guha, A., 2008, "Transport and deposition of particles in turbulent and laminar flow," *ARFM*, **40**, pp. 311–341.
- [16] Yeung, P. K., and Pope, S. B., 1989, "Lagrangian statistics from direct numerical simulations of isotropic turbulence," *J. Fluid Mech.*, **207**, p. 531–586.
- [17] Jie, Y., Cui, Z., Xu, C., and Zhao, L., 2022, "On the existence and formation of multi-scale particle streaks in turbulent channel flows," *J. Fluid Mech.*, **935**, p. A18.
- [18] Xiao, W., Jin, T., Luo, K., Dai, Q., and Fan, J., 2020, "Eulerian–lagrangian direct numerical simulation of preferential accumulation of inertial particles in a compressible turbulent boundary layer," *J. Fluid Mech.*, **903**, p. A19.
- [19] Chen, G., Wang, H., Luo, K., and Fan, J., 2022, "Two-way coupled turbulent particle-laden boundary layer combustion over a flat plate," *J. Fluid Mech.*, **948**, p. A12.
- [20] Yu, M., Zhao, L., Yuan, X., and Xu, C., 2024, "Transport of inertial spherical particles in compressible turbulent boundary layers," *J. Fluid Mech.*, **990**, p. A5.
- [21] Crowe, C. T., Schwarzkopf, J. D., Sommerfeld, M., and Tsuji, Y., 2011, *Multiphase Flows with Droplets and Particles* CRC Press.
- [22] Hussein, M. F., and Tabakoff, W., 1973, "Dynamic behavior of solid particles suspended by polluted flow in a turbine stage," *J. Aircraft*, **10**(7), pp. 434–440.
- [23] Elfeki, S., and Tabakoff, W., 1987, "Erosion study of radial flow compressor with splitters," *ASME J. Turbomach.*, **109**(1), 01, pp. 62–69.
- [24] Elghobashi, S., 1994, "On predicting particle-laden turbulent flows," *Appl. Sci. Res.*, **52**(4), p. 309–329.
- [25] Ghenaïet, A., 2012, "Study of sand particle trajectories and erosion into the first compression stage of a turbofan," *ASME J. Turbomach.*, **134**(5), 05, p. 051025.
- [26] Vogel, A., Durant, A. J., Cassiani, M., Clarkson, R. J., Slaby, M., Diplas, S., Krüger, K., and Stohl, A.,

- 2018, "Simulation of volcanic ash ingestion into a large aero engine: Particle–fan interactions," *ASME J. Turbomach.*, **141**(1), 11, p. 011010.
- [27] Sandberg, R. D., and Michelassi, V., 2022, "Fluid dynamics of axial turbomachinery: Blade- and stage-level simulations and models," *Ann. Rev. Fluid Mech.*, **54**, pp. 255–285.
- [28] Beck, A., Ortwein, P., Kopper, P., Kraiss, N., Kempf, D., and Koch, C., 2019, "Towards high-fidelity erosion prediction: On time-accurate particle tracking in turbomachinery," *Int. J. Heat Fluid Flow*, **79**, p. 108457.
- [29] Armenio, V., Piomelli, U., and Fiorotto, V., 1999, "Effect of the subgrid scales on particle motion," *Phys. Fluids*, **11**(10), 10, pp. 3030–3042.
- [30] Kuerten, J. G. M., and Vreman, A. W., 2004, "Can turbophoresis be predicted by large-eddy simulation?," *Phys. Fluids*, **17**(1), 11, pp. 011701–011701–4.
- [31] Oka, Y., and Yoshida, T., 2005, "Practical estimation of erosion damage caused by solid particle impact: Part 2: Mechanical properties of materials directly associated with erosion damage," *Wear*, **259**(1), pp. 102–109.
- [32] Zaki, T. A., Wissink, J. G., Rodi, W., and Durbin, P. A., 2010, "Direct numerical simulations of transition in a compressor cascade: the influence of free-stream turbulence," *J. Fluid Mech.*, **665**, p. 57–98.
- [33] Sandberg, R. D., Michelassi, V., Pichler, R., Chen, L., and Johnstone, R., 2015, "Compressible direct numerical simulation of low-pressure turbines-part i: Methodology," *ASME J. Turbomach.*, **137**(5), p. 051011.
- [34] Deuse, M., and Sandberg, R. D., 2020, "Implementation of a stable high-order overset grid method for high-fidelity simulations," *Comp. Fluids*, **211**, p. 104449.
- [35] Klein, M., Sadiki, A., and Janicka, J., 2003, "A digital filter based generation of inflow data for spatially developing direct numerical or large eddy simulations," *J. Comp. Phys.*, **186**, pp. 652–665.
- [36] Toubert, E., and Sandham, N. D., 2009, "Large-eddy simulation of low-frequency unsteadiness in a turbulent shock-induced separation bubble," *Theor. Comput. Fluid Dyn.*, **23**, pp. 79–107.
- [37] Sandberg, R. D., and Sandham, N. D., 2006, "Nonreflecting zonal characteristic boundary condition for direct numerical simulation of aerodynamic sound," *AIAA J.*, **44**, pp. 402–405.
- [38] Elghobashi, S., and Truesdell, G. C., 1992, "Direct simulation of particle dispersion in a decaying isotropic turbulence," *J. Fluid Mech.*, **242**, p. 655–700.
- [39] White, F. M., 1991, *Viscous fluid flow* McGraw-Hill, New York.
- [40] Wen, C. Y., and Yu, Y. H., 1966, "Mechanics of fluidization," *Chemical Engineering Progress Sympo-*

sium Series, **62**, pp. 100–111.

- [41] Saffman, P. G., 1965, “The lift on a small sphere in a slow shear flow,” *J. Fluid Mech.*, **22**(2), p. 385–400.
- [42] Saffman, P. G., 1968, “The lift on a small sphere in a slow shear flow - corrigendum,” *J. Fluid Mech.*, **31**(3), p. 624–624.
- [43] Tartakovsky, A., and Meakin, P., 2005, “Modeling of surface tension and contact angles with smoothed particle hydrodynamics,” *Phys. Rev. E*, **72**, Aug, p. 026301.
- [44] Tartakovsky, A. M., and Panchenko, A., 2016, “Pairwise force smoothed particle hydrodynamics model for multiphase flow: Surface tension and contact line dynamics,” *J. Comp. Phys.*, **305**, pp. 1119–1146.
- [45] Norouzi, H. R., Zarghami, R., Sotudeh-Gharebagh, R., and Mostoufi, N., 2016, *Coupled CFD-DEM modeling: formulation, implementation and application to multiphase flows* John Wiley & Sons.
- [46] Wang, T., Meng, B., Tian, B., and Zhao, Y., 2026, “A high-fidelity framework for point-particle direct numerical simulation based on multi-block overset grids,” *Comput. Phys. Commun.*, **322**, p. 110059.
- [47] Bansal, N. P., and Choi, S. R., 2015, “Properties of cmas glass from desert sand,” *Ceram. Int.*, **41**(3, Part A), pp. 3901–3909.
- [48] Lardeau, S., Leschziner, M., and Zaki, T., 2012, “Large eddy simulation of transitional separated flow over a flat plate and a compressor blade,” *Flow Turbul. Combust.*, **88**(1), pp. 19–44.
- [49] Scillitoe, A. D., Tucker, P. G., and Adami, P., 2016, “Numerical investigation of three-dimensional separation in an axial flow compressor: The influence of freestream turbulence intensity and endwall boundary layer state,” *ASME J. Turbomach.*, **139**(2), p. 021011.
- [50] Scillitoe, A. D., Tucker, P. G., and Adami, P., 2019, “Large eddy simulation of boundary layer transition mechanisms in a gas-turbine compressor cascade,” *ASME J. Turbomach.*, **141**(6), p. 061008.
- [51] Hunt, J. C. R., Wray, A. A., and Moin, P., 1988, “Eddies, streams, and convergence zones in turbulent flows,” In *Studying Turbulence Using Numerical Simulation Databases*, 2, Vol. 1, Center for Turbulence Research Report CTR-S88, pp. 193–208.
- [52] Nolan, K. P., and Zaki, T. A., 2013, “Conditional sampling of transitional boundary layers in pressure gradients,” *J. Fluid Mech.*, **728**, pp. 306–339.
- [53] Marxen, O., and Zaki, T. A., 2019, “Turbulence in intermittent transitional boundary layers and in turbulence spots,” *J. Fluid Mech.*, **860**, pp. 350–383.
- [54] Otsu, N., 1979, “A threshold selection method from gray-level histograms,” *IEEE Trans. Syst. Man Cybern.*, **9**, pp. 62–66.
- [55] Sardina, G., Schlatter, P., Brandt, L., Picano, F., and Casciola, C. M., 2012, “Wall accumulation and

spatial localization in particle-laden wall flows," *J. Fluid Mech.*, **699**, p. 50–78.